WILEY

FFEMS Fatigue & Fracture of Engineering Materials & Structures

ORIGINAL ARTICLE OPEN ACCESS

Natural Seawater Impact on Crack Propagation and Fatigue Behavior of Welded Nickel Aluminum Bronze

T. H. E. Dobson[1] | P. Wilson[2] | N. O. Larrosa[1,3] | M. Williams[2] | H. E. Coules[1]

[1]Solid Mechanics Research Group, University of Bristol, Bristol, UK | [2]Warwick Manufacturing Group, University of Warwick, Warwick, UK | [3]TECNALIA R&I, Basque Research and Technology Alliance (BRTA), Donostia-San Sebastián, Gipuzkoa, Spain

Correspondence: T. H. E. Dobson (tamsin.dobson@bristol.ac.uk)

ABSTRACT

Nickel aluminum bronze (NAB) is a complex alloy used extensively in the marine environment. Fatigue strength of NAB is reduced by welding and prior seawater corrosion. This study investigated the combined effect of corrosion and plasma welding on the fatigue behavior of NAB. Natural seawater corroded samples were used in tension-tension cyclic loading tests to observe fatigue crack initiation, propagation, and failure. Fatigue cracks initiated from corrosion pits at the weld toe. Stress corrosion and fatigue cracks propagated along the path of β' and κ_{III} phases. A short crack growth model (SCGM) predicted fatigue strength using experimentally obtained material properties and corrosion pit dimensions. Model predictions were used to develop S-N curves and were within 30% of experimental results. The SCGM produced accurate and reliable fatigue life results that could be applied by industry to aid in revalidation decision making and inspection scheduling.

1 | Introduction

Fatigue-initiated failures at weldments continue to be a frequent root cause of marine vessel loss and death at sea. For example, the fishing vessel *Ocean Quest* suffered a hull weld failure causing the loss of the vessel in 2019 [1] and a weld was the root cause of an uncontrolled fire that spread through the ferry *Dieppe Seaways* in 2014 [2]. Because of this, the International Maritime Organization (IMO) is putting a higher priority on the through-life sustainability and safety of welded components while also pushing the marine industry to build and operate more energy-efficient vessels, with operators becoming more environmentally aware.

1.1 | Welded Nickel Aluminum Bronze

Nickel aluminum bronze (NAB) is a multiphase copper alloy used extensively in the marine industry, most commonly in valves, manifolds, and propellors. It often forms safety-critical parts and currently falls under tight restrictions in accordance with Defense Standard 02-747 Part 2 [3] when welding is required to components that come into contact with seawater during service (wetted components). As such, there is a strong need for updated guidance on the use of welding to repair wetted NAB components.

In welded NAB, the heat-affected zone (HAZ) has been identified as a common failure point [4], so welding process development usually focuses on reducing the HAZ width [5, 6]. Plasma welding was identified as the most favorable candidate process for use with NAB for this research, and it has been shown to produce a small HAZ width [6].

NAB forms a complex microstructure whereby small variations in composition or heat treatment (HT) can alter the corrosion resistance of the material [7]. Previous research has characterized

---

Summary

- Combined effect of corrosion and plasma welding on fatigue behavior
- Fatigue crack initiation from corrosion pits
- Fatigue crack propagation along the path of the β' and κ_{III} phases
- Microstructural short crack model predicts fatigue strength and is used to develop S-N curves

NAB microstructure and phase transformations that result from different processing schedules (e.g., [8–10]). The key phases of welded NAB manufactured to Defense Standard 02-747 Part 2 [3] are summarized in Table 1, and NAB is characterized in Section 3.4.

1.2 | Effect of Welding and Heat Treatment on Fatigue

Cyclic loading results in crack initiation and propagation when plastic strains (produced by cyclic stress) cause crack initiation and tensile stresses force crack propagation [18]. The number of cycles to failure for different cyclic stress levels can be represented by an S-N curve. Established S-N curves for cast NAB show high cycle numbers before failure with a reduction in fatigue strength seen for corroded samples [19, 20]. Holtam et al. [21] suggested a best practice guide for evaluating knockdown factors (KDFs) that describe the fatigue strength of corroded material in terms of the fatigue strength of the parent material. They noted that, in instances where the slope of the S-N curve differs, the KDF will vary depending on the stress range. For these scenarios, they suggested a method that involves the calculation of the KDFs, as the ratio of the parent life divided by the life of the corroded sample, at the extreme test stresses. This produces maximum and minimum (i.e., a range of) KDFs that could then be used to calculate a mean KDF.

The results shown in [20] highlight the ability of HT to improve NAB fatigue life. For NAB components used in UK military vessels, the HT requirements are specified in Defense Standard 02-747 Part 2. The limitations of industry-standard nondestructive test (NDT) detectors mean that cracks must have propagated before detection is possible. Because of this, it is important to understand the propagation mechanism so that NDT inspection can be focused on areas of likely cracking.

1.3 | Effect of Corrosion on Fatigue

Corrosion is known to affect the fatigue behavior of welded structures [22, 23]. In weldments, fatigue cracks commonly initiate at the weld toe (WT) and propagate to a final fracture [24]. This is due to the weld bead acting as a geometric discontinuity that produces a nonlinearity in the stress distribution and makes surface defects at the WTs more likely to cause crack initiation [25]. Similarly, fatigue cracks can initiate from corrosion pits [26–29], so corrosion pits at the WT significantly affect fatigue life.

Previous research [30, 31] has shown that, for high-cycle fatigue initiating from corrosion pits, a significant proportion of fatigue life is consumed in the pit-to-crack transition and in the short crack regime. In this research, a short crack growth model

TABLE 1 | Key phases identified in NAB manufactured to Defense Standard 02-747 Part 2 plus the additional retained phase found in welded NAB.

Phase	Phase description
α	This is the dominant phase in NAB consisting of a coarse field, face-centered-cubic (FCC), Cu-rich phase with Widmanstätten morphology [11].
κ_I κ_{II} κ_{III} κ_{IV}	There are four types of Fe-, Ni-, and/or Al-rich intermetallic phases [12]. These phases improve the mechanical properties of the material and increase the amount of aluminum that can be included in the material before the β phase transforms into the (less desirable) γ phase [13]. The κ_I phase is a rosette-shaped Fe-rich phase that forms at the α grain centers. This phase is only found occasionally in localized events where local Fe content exceeds 5 wt% [14]. The κ_{II} phase (which is based on Fe_3Al) tends to be distributed (unevenly) at the α boundary in the form of small rosettes (relative to the rosettes of the κ_I phase). The κ_{IV} phase is also Fe rich and is found as a fine, spheroidal precipitate within the α phase [15]. The κ_{III} phase is eutectoid and forms continuous (lamellar) networks at the α phase and κ_I phase grain boundaries [16]. It is based on NiAl, so is nickel rich. It forms as a result of the eutectoid transformation when the β phase breaks down and is therefore the predominant intermetallic phase.
β'	The β' phase is a body-centered-cubic (BCC), island martensite, high-temperature phase, which is also Cu rich but with a smaller percentage composition of Ni and Fe. It is considered undesirable because of its susceptibility to corrosion, and the complete eradication of this phase in cast NAB can only be achieved if the cooling time is sufficiently long so that complete eutectoidal decomposition of the β' phase occurs [17]. NAB manufactured to Defense Standard 02-747 Part 2 [3] would not usually contain this phase; however, it can be retained in the weld material and HAZ of welded NAB [16].

(SCGM) is used to predict the fatigue life of corroded NAB. The advantage of the short crack microstructural model is that it effectively describes the microscale mechanisms while only requiring a minimal number of input parameters. This makes it a more plausible solution to be used by industry while maintaining accuracy. In addition, it is run from MATLAB, which is a software that is easily available to industry and one that many engineers are able to code (e.g., [32]).

1.4 | Predicting Fatigue Behavior of Corroded, Welded NAB

Classical fatigue life estimation models include classical stress-, strain-, or strain energy–based models. Most models are based on either mesoscale factors or microscale factors. Microscale techniques are arguably more accurate in modeling crack propagation; however, it is difficult to identify and measure microscale damage using off-the-shelf equipment available to industry. As such, some fatigue life prediction models aim to link mesoscale and microscale damage, for example, [33]. This has the potential to show crack growth direction but is complicated to apply and therefore unlikely to be taken up by industry.

The Navarro and de los Rios (NR) model [34] is a mechanism-based SCGM that uses the distribution of grain boundaries to estimate fatigue life. It is based on evidence given by [35] and [36] and follows the process given by [37] and [38] assuming that the plastic zone at the crack tip of short cracks is confined by grain boundaries. As such, the model considers grain boundaries as the slip barriers of a specific strength that is determined by the strength needed to form a new slip band in the next grain. In this way, the NR model [34] takes account of the typical temporary halt features of short crack growth by including the discrete jumps in plastic slip at each grain boundary. The NR model uses the Kitagawa–Takahashi (K-T) diagram [39] (Figure 1) to calculate the strength of each grain

boundary barrier. The K-T diagram encapsulates fracture mechanics and stress-based approaches and illustrates the far-field stress amplitude ($\Delta\sigma_{th}^{\infty}$) against the crack length (a), where $\Delta\sigma_0$ = defect-free material fatigue limit. Below the crack length (a_0), cracks are considered to be short, whereas when $a > a_0$, cracks are long. a_0 is often denoted as El Haddad intrinsic crack length (Equation 1).

$$a_0 = \frac{1}{\pi}\left(\frac{\Delta K_{th}}{\Delta\sigma_0}\right)^2 \tag{1}$$

However, Chapetti [41] showed that the El Haddad correction is nonconservative and instead suggested that as short cracks do not show complete crack closure during the fatigue cycle, the threshold of stress intensity range is significantly smaller for short cracks. The slope in the long crack regime is described by Equation (2). Below this slope, a crack should not grow (according to the LEFM assumptions). For small cracks, experimental results (solid line in Figure 1) tend to deviate from the dashed lines.

$$\Delta K = \Delta\sigma_{th}Y\sqrt{\pi a_{th}} \tag{2}$$

The SCGM approach introduced in [42] is based on this NR model. The K-T diagram can therefore be output from the SCGM model and predict the effect of corrosion pits on the fatigue strength of the material under consideration.

In a sample that is not corrosion pitted, the stress required to overcome the first grain boundary is the same as the stress required to propagate through all the microstructural barriers, and therefore, the fatigue strength of the uncorroded sample is equal to the stress required to overcome the first grain boundary. However, this is not the case for corroded samples.

Corrosion pits are known stress raisers, and so cracks that initiate from a pit will require a lower stress gradient to pass through
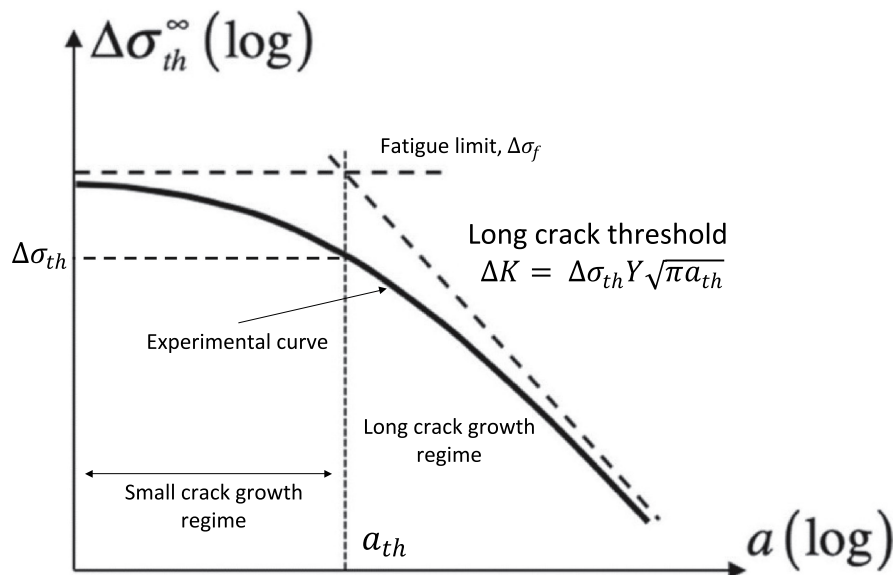

FIGURE 1 | Kitagawa–Takahashi (K-T) diagram schematic showing the far-field stress range ($\Delta\sigma_{th}^{\infty}$) against crack length ($a$). Adapted from [40]. [Colour figure can be viewed at wileyonlinelibrary.com]

the first few grain boundaries (while still within the stress concentration region). As such, there are some instances where cracks that initiate from corrosion pits arrest within the first few grain boundaries as they cannot overcome the full stress gradient outside of the stress concentration region created by the corrosion pit.

The SCGM approach is based on the assumption that cracks initiate from the corrosion pits and uses a relationship between the grain barrier strength of the nonpitted and pitted components. This means that the fatigue strength of the pitted component can be calculated as the maximum value of the computed fatigue strength in the output K-T diagram [42, 43]. Using this approach, it is possible to build up a predictive S-N curve for a pitted material using the SCGM approach.

The aim of this paper is to determine the effect of plasma welding and corrosion (in the presence and absence of biofouling) on the fatigue behavior of NAB and to describe the crack propagation mechanism. This understanding will enable the development of a predictive model for the fatigue life of welded and corroded NAB. The objectives are to investigate crack initiation and propagation, determine the effect of (natural and simulated) seawater corrosion on fatigue behavior, and produce fatigue life predictive models for welded NAB that has corroded in the presence of biofouling organisms in natural seawater.

The results and predictive model presented in this study should be used to improve predictive maintenance so that unexpected component failure can be prevented. This is especially important for welded NAB components that are commonly used on marine vessels where their failure could cause loss of life and/or loss of the vessel.

2 | Materials and Method

2.1 | Overview

Uncorroded and corroded plasma welded NAB was cut to produce cross-weld fatigue samples. Some of the welded samples were fatigued to allow crack propagation but stopped before failure. X-ray computed tomography (CT) and microscopy outputs of these cracked samples show intragranular propagation following the κ_{III} phase. S-N curves of the parent and welded samples were created, and the effect of the plasma weld was to reduce the number of cycles required before failure. The S-N curves created by corroded samples were used to calculate knockdown factors required to account for the effect of corrosion on fatigue life. The fatigue test data were used to inform an SCGM that enabled the prediction of fatigue life for corroded samples at a range of stress amplitudes.

2.2 | Fatigue Samples

NAB coupons were saw cut from a rod that conformed to Defense Standard 02-747 Part 2 [1] with a minimum of 250 MPa 0.2% proof strength and a tensile strength of at least 620 MPa. The NAB had a chemical composition of 9.89% Al, 3.75% Fe, 4.71% Ni, and 81.66% Cu, wt% as described in [6], supporting the results of [10, 44–46], and the microstructure is shown in Figure 2.

The NAB coupons were 200-mm diameter, 30-mm sections with two Ø 10-mm drill holes to allow easier manipulation. Plasma welding was carried out at Cranfield University using the parameters shown in Table S1 including 100% argon gas shielding. A bead on plate weld was created between the two drill holes as per Figure 3a. The wire used was SIFMIG 44 (Cu6328 EN 14640). Optical microscopic images of the cross section of the weld clearly show the different microstructures in the parent material, HAZ, and weld material (WM; Figure 4).

In the as-welded condition, the average weld bead height and width ($\pm$ standard deviation, SD) were 1.84 mm $\pm$ 0.13 mm and 7.51 mm $\pm$ 0.29 mm, respectively ($n = 25$). The welds showed good penetration and represented welds that would pass industry standard inspections.

As described in [48] and summarized in Data S1, the welded coupons were immersed for 12 or 18 months in one of three environments: natural seawater, simulated seawater (SSW), or air. Uncorroded and (after environmental exposure) corroded
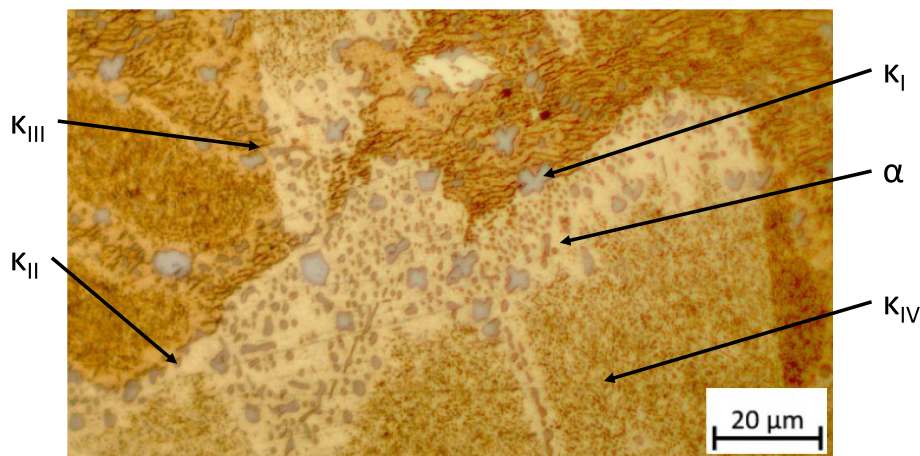

FIGURE 2 | Optical microscope image of nickel aluminum bronze after etching with FeCl$_3$ solution. The lack of γ and β phases in the parent material is consistent with the HT carried out on the cast material [47]. [Colour figure can be viewed at wileyonlinelibrary.com]
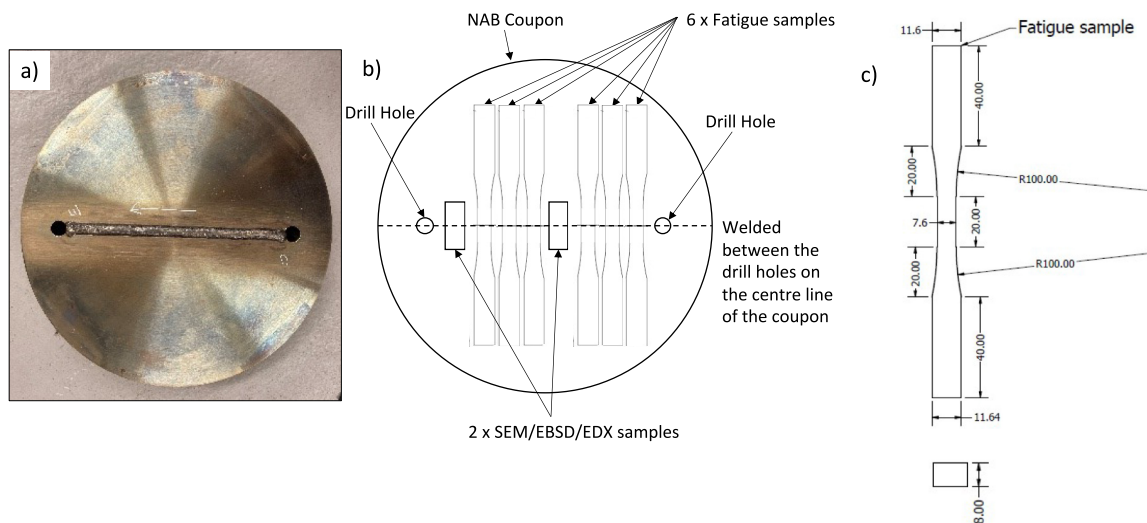
FIGURE 3 | (a) Plasma weld on an NAB coupon that was randomly chosen to manufacture six fatigue samples and a cross-sectional SEM sample as per (b). The detailed geometry of the fatigue samples is shown in (c). [Colour figure can be viewed at wileyonlinelibrary.com]
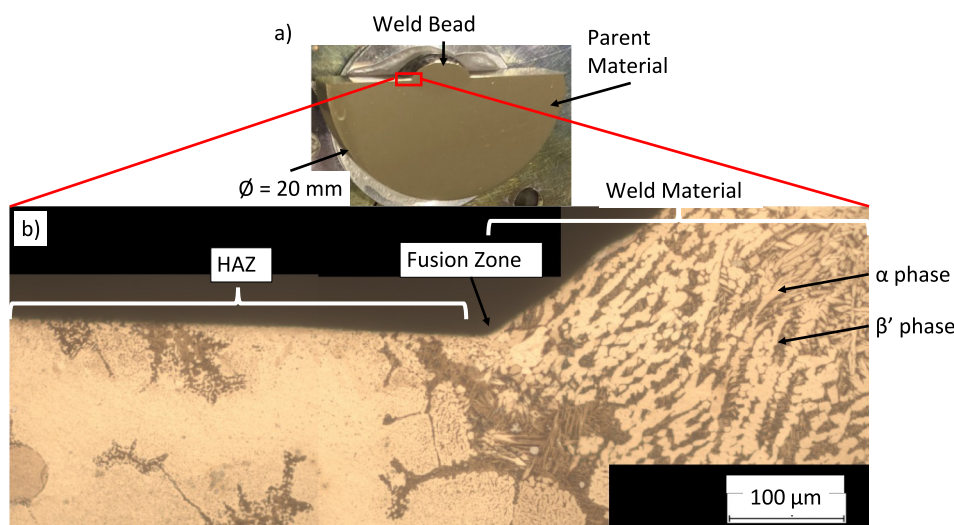

FIGURE 4 | (a) Weld cross-section sample and (b) weld toe showing the difference in the microstructure between the weld material (WM) and material in the heat-affected zone (HAZ). This image also clearly shows the fusion zone (FZ) that is predominantly composed of the α and β′ phases but also contains some of the κ phases. The dark-colored phase is the retained β′ phase (seen in the WM and HAZ). [Colour figure can be viewed at wileyonlinelibrary.com]

samples were cut (as per Figure 3b,c) to create across-weld fatigue samples.

Most fatigue samples were tested with the weld bead intact. However, to investigate the effect of weld bead geometry on fatigue strength, five uncorroded welded samples were randomly selected to have the weld bead ground down. These samples only had a small amount of smoothed WM (with a height of 0.4 mm ± 0.1 mm) but retained the HAZ.

Nine types of fatigue samples were created: parent (uncorroded) ($n = 9$), welded (uncorroded) ($n = 12$), welded (uncorroded, no weld bead) ($n = 5$), 12-month natural seawater immersed ($n = 22$), 18-month natural seawater immersed ($n = 22$), 12-month SSW immersed ($n = 8$), 18-month SSW immersed ($n = 9$), 12-month air exposed ($n = 4$), and 18-month air exposed ($n = 4$).

2.3 | Interrupted Fatigue Crack Growth Tests

Previous fatigue studies on corroded NAB have shown that the effect of frequency on corrosion fatigue strength is insignificant [20, 49, 50] when considering high-frequency fatigue states. Therefore, once initial fatigue tests were completed at a frequency (f) of 10 Hz, subsequent tests were completed at 20 Hz to save time. The interrupted fatigue crack growth tests were carried out on samples with different crack lengths, and the propagated cracks were then visualized using x-ray CT.

X-ray CT was performed using the scan settings shown in Table 2 and was used to visualize internal cracks in the NAB samples. X-ray CT scanning is nondestructive, reveals internal structure, and provides 3D spatial data [51]. The central part of six fatigued samples was scanned, covering the central straight

TABLE 2 | X-ray CT scan settings.

Methodology	Details	
Equipment used	Zeiss Metrotom 1500	
Software used	MetrotomOS, Avizo 3D 2021.2, and VGStudio Max 2.2	
Conditions	Exposure voltage (kV)	180
	Exposure power (W)	15.3
	Exposure time (s)	2
Filters	Material	Copper
	Thickness (mm)	1
Information about the scan	Voxel size (μm)	15.19
	No. of projections	1700–1750
	Source-detector distance (SDD) (mm)	1448
	Frame per projection	2–3
	Voxel scaling correction	No

TABLE 3 | Fatigue method for x-ray CT scan samples.

Welded fatigue sample	Cycle number	Increase in extension (compared with initial crosshead displacement)	Peak stress ($R = 0.1$)
X1	Stop when crosshead position changes by more than 0.5 mm from unloaded state.	67%	0.9 $\sigma_{0.2}$
X2	Stop when crosshead position changes by more than 0.4 mm from unloaded state.	33%	
X3	Stop when crosshead position changes by more than 0.3 mm from unloaded state.	0%	
X4	Stop when crosshead position changes by more than 0.35 mm from unloaded state.	17%	
X5	None—Reference sample	N/A	N/A
X6	None—Reference sample (end of weld)	N/A	

edge area in order to avoid missing any damage in the samples including crack geometries, porosity, material phases, and their spatial relationships.

From observing initial cyclic behavior of all the NAB parent samples tested ($n = 3$), an initial maximum crosshead displacement of 0.3 mm was measured (over the first 200,000 cycles). A clear extension of approximately 0.2 mm was observed to occur approximately 300 cycles before failure in the failed samples. As such, a total extension of over 0.5 mm (representing > 67% increase in extension compared with the initial maximum extension) was found to result in fracture. With this information in mind, samples with unfailed, propagated cracks were created as per Table 3 to create a variety of crack lengths (see Data S2 for further information). Peak stress is shown as a fraction of minimum specified yield stress ($\sigma_{0.2}$), which was 250 MPa according to Defense Standard 02-747 Part 2 [3]).

The cracked samples were imaged using SEM, EBSD (FEI Quanta 200 FEG-SEM), and optical microscopy (Zeiss Brightfield Optical Microscope). Etching with aqueous solutions of $FeCl_3$ and HCl allowed the visualization of the propagation mechanism using an optical microscope.

The side of two (corrosion pitted) 12-month natural seawater immersed fatigue samples was polished to 0.06 μm (using ChemoMet Colloidal Silica). These two samples were imaged using SEM (FEI Quanta 200 FEG-SEM) and then fatigued at a peak tensile stress of 220 MPa ($R = 0.1$, 20 Hz) using an Instron 1341, where the peak tensile stress was calculated using the uncorroded cross-sectional area. Based on the results from Table 3, the fatiguing was automatically stopped when the crosshead position changed by more than 0.4 mm from the unloaded state. The samples were then re-imaged using SEM so that the fatigue crack initiation and propagation could be analyzed. This enabled a detailed understanding of fatigue crack initiation from corrosion pits.

2.4 | S-N Curve Determination

The method used to create the S-N curves was based on the method published by Nakazawa and Kodama [52] (which is an English translation of sections 2 and 5.1 of JSME, Standard Method of Statistical Fatigue Testing, JSME S 002, 1981) using a stress ratio, $R = 0.1$ and frequency, $f = 20\,Hz$. The method was adapted to enable additional fatigue tests to be undertaken where large variation in cycles to failure was seen and to reduce unnecessary experimental repeats. The applied peak cyclic stress (and stress range) was calculated from the applied maximum load (and load range) using the uncorroded fatigue sample area.

The effect of reduction in wall thickness was considered by comparing the uncorroded and corroded experimental results on an S-N curve along with the corroded experimental results when the engineering stress (σ) was re-calculated (σ_{WR}) assuming that the "wall thickness" (T) was reduced by the depth of the deepest corrosion pit measured at the WT of each fatigue sample (d) (Equation 3).

$$\sigma_{WR} = \frac{T\sigma}{T - d} \tag{3}$$

The deepest corrosion pit depth (d) was measured in 3D using the Alicona Infinity Microscope. As such the maximum depth of the corrosion pit is taken to produce the worst-case wall thickness reduction.

KDFs for the different subsets were calculated relative to the uncorroded welded case, and the uncorroded welded case was itself compared with the uncorroded parent material.

As per Method 2 described by Holtam et al. [21], S-N curve KDFs were calculated at the maximum and minimum stress ranges for which test data were available in each case. For calculating

the KDF between parent and welded samples, the minimum and maximum stresses used were 350 and 185 MPa. For KDFs calculated for corroded welded samples compared with uncorroded welded samples, the minimum and maximum stresses used were 220 and 182 MPa. These ranges used for fitting the KDFs are representative of high cycle fatigue service loading (with number of cycles between 10^4 and 10^7), which is the same cycle range used in BS 7608 [53] to calculate KDFs for steel products used in seawater applications.

Taking the welded cases as an example, the number of cycles to failure at the minimum and maximum stress range was calculated from the linear regression models of the experimental results for the corroded case ($N_{c,\,min}$ and $N_{c,\,max}$) and the uncorroded case ($N_{w,\,min}$ and $N_{w,\,max}$). The minimum and maximum KDFs were calculated from these using Equation (4). The KDF for each corroded case was calculated as the mean of the KDF_{min} and KDF_{max} in each case.

$$
\begin{aligned}
KDF_{min} &= \frac{N_{c,min}}{N_{w,min}} \\
KDF_{max} &= \frac{N_{c,max}}{N_{w,max}}
\end{aligned} \tag{4}
$$

2.5 | Short Crack Microstructural Method

The Navarro and de los Rios short crack microstructural method [34, 54, 55] was used to consider the effect of natural seawater-induced surface corrosion on early crack propagation from corrosion pits. For the sake of brevity, the mathematical formulation of the methodology is not described here, and the reader can refer to the paper by Balbin et al. [42].

The SCGM is coded in MATLAB and uses the fatigue strength identified by fatigue experiments, average grain size identified

TABLE 4 | Input parameters used for predicting S-N curves of pitted NAB via the model of Balbin et al. [42].

Parameter	Input			Reference
Grain size	65 µm			[56]
Threshold SIF (K_{th})	4.4–7.4 MPa m$^{1/2}$			[57]
Fatigue strength (σ)	220 MPa (3×10^4 cycles), 182 MPa (2×10^5 cycles), 156.5 MPa (8×10^5 cycles) and 122 MPa (5×10^6 cycles)			Current research data ($n = 12$ for welded, uncorroded samples)
Pit details	Sample no. (showing months immersed)	Depth (mm)	Width (mm)	Current research data. Note that Samples A–E are ($n = 5$) individual fatigue samples. For "Deep" pit samples, $n = 21$
	A (18)	0.738	3.12	
	B (18)	0.645	3.106	
	C (18)	0.578	4.464	
	D (12)	0.566	3.962	
	E (12)	0.355	2.924	
	"Deep" pits	≥ 0.35 mm	Various	

using EBSD methods described in [56], and the long crack threshold stress intensity factor range (K_{th}) [57].

The input parameters were taken from previous research and current experimental data, Table 4, using a parametric algorithm tool to create 2D notches that were coded in the SCGM as described in [34, 42, 58]. The model was used to estimate pitting corrosion fatigue strength and S-N curves, and this output was compared with experimental data.

The methodology uses the K-T diagram of the material. The micromechanical approach is integrated into a numerical framework that models the pit geometry, the crack, and the microstructural barriers by means of distributed dislocations and uses a K-T diagram to account for the effect of the environment on the material's microstructure resistance for short and long crack propagation. The novelty of the application of the model in this paper lies in the use of a K-T diagram specific for each fatigue life shown in Table 3.

WT corrosion pit geometry was measured through 3D scans using an Alicona Infinite Focus microscope (Alicona Imaging GmbH, Graz, Austria) with a vertical resolution of 7 μm and lateral resolution of 17 μm. The WT corrosion pit depths and widths stated in Table 4 are for the deepest pits observed in each sample.

From these inputs, the SCGM model predicts fatigue strength assuming that the input pit geometry is the "killer pit" (which is reasonable as they were the deepest pits at the WT in each case). From these predictions, S-N curves for specified pit geometry can be produced.

3 | Results

3.1 | Uncorroded Sample Crack Initiation and Propagation

The uncorroded, welded samples all failed at the WT. Optical microscope images show cracks initiating between the HAZ of the parent material running perpendicularly into the material (Figure 5). Intragranular crack propagation is observed through the large grains of the parent material. They also show cracks tending to propagate through areas of κ_{III} phases (Figure 6), which explains the complexity of the crack geometry seen in x-ray CT images (Figure 7).

Porosity was found to be insignificant and is therefore not considered further. Information is available in Data S3.

SEM fractography shows that, in the areas of fast fracture, the SEM images show dimples with varying shapes and ratchet marks (Data S4 and Figure S5).

3.2 | Crack Initiation and Propagation in Corroded Samples

As with the uncorroded, welded samples, the corroded welded samples all failed at the WT. Corrosion pits found at the WT of samples immersed in natural seawater for 12 months were imaged before and after fatiguing to establish crack initiation and propagation mechanisms (Figure 8).
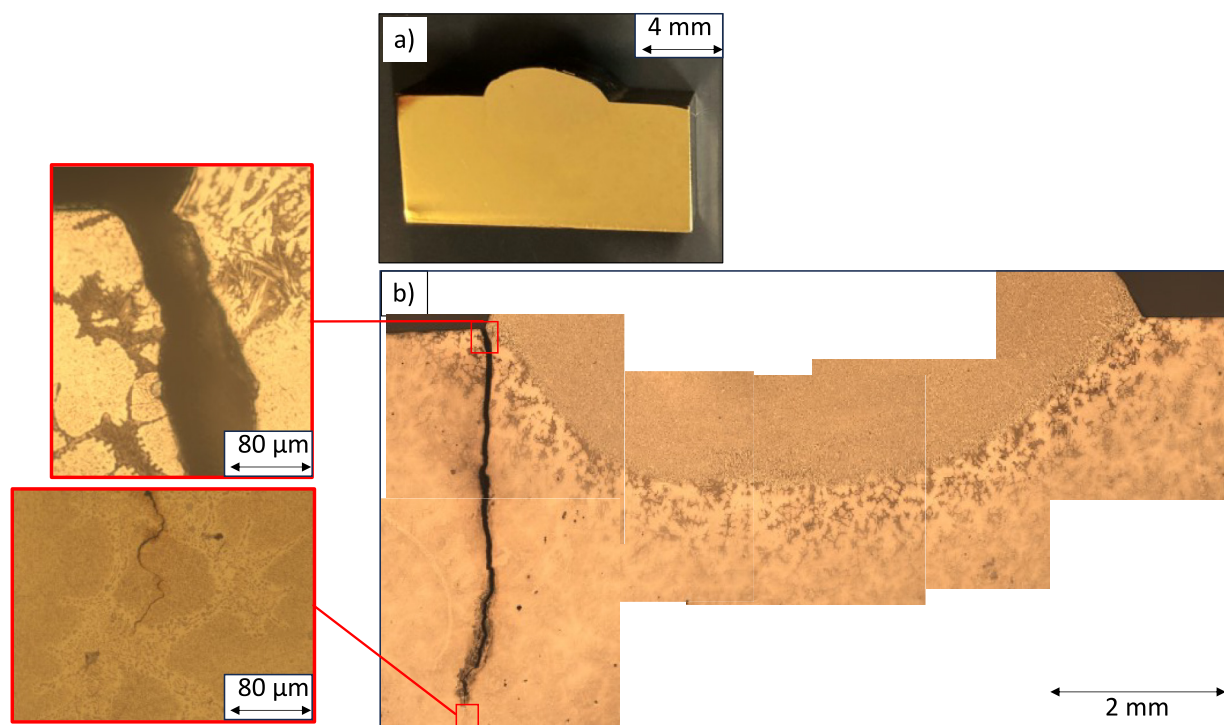

FIGURE 5 | (a) Sample showing crack at the weld toe caused by fatigue. (b) Etched optical image looking at the side of the weld bead where a fatigue crack has initiation at the weld toe and propagated into the parent material with magnified images of the weld toe and crack tip. [Colour figure can be viewed at wileyonlinelibrary.com]
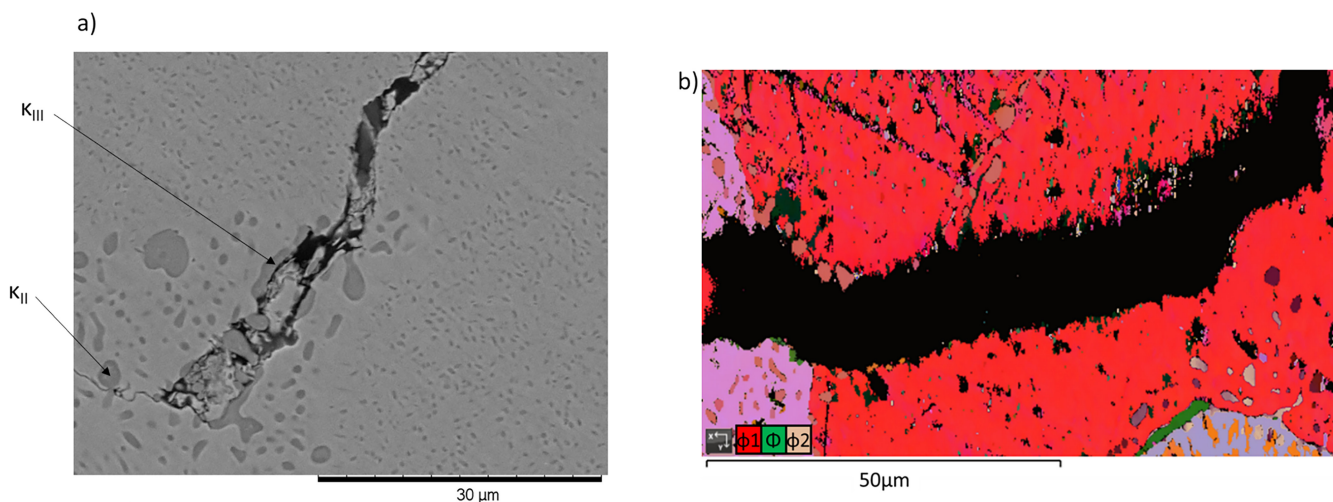
FIGURE 6 | (a) SEM image showing crack tip propagating through areas dense with κ phases. (b) Euler color image where fragments of smaller phases are seen around the edges of a wider portion of the crack. [Colour figure can be viewed at wileyonlinelibrary.com]
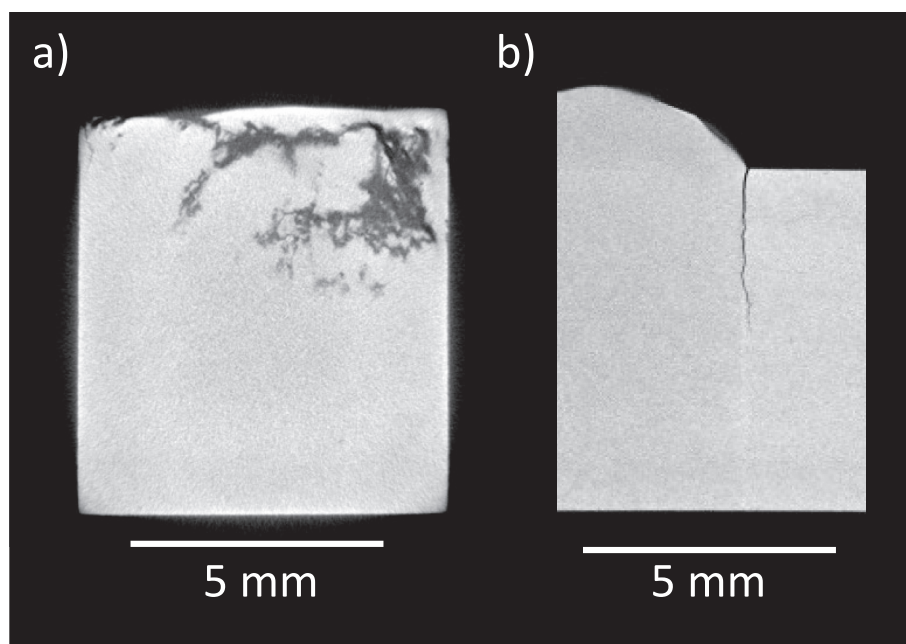

FIGURE 7 | X-ray CT scan outputs from sample X2 showing (a) horizontal cross section at the weld toe showing the crack geometry and (b) central vertical cross section showing crack geometry at the weld toe.

For two samples, fatigue tests were carried out at a peak stress of 220 MPa ($R = 0.1$, $f = 20$ Hz) and stopped once the crosshead extension (x_{CH}) = 0.4 mm (based on the results shown in Table 3). The extent of corrosion out from the WT (w) and maximum corrosion depth (d) for the samples were $w_1 = 1.0261$ mm, $d_1 = 0.394$ mm and $w_2 = 2.644$ mm, $d_2 = 0.138$ mm. Hence, one of the samples exemplified a shallow WT corrosion pit, whereas the other had a deep WT corrosion pit.

Figure 8 shows the prefatigued and postfatigued SEM images for the sample with the deep WT corrosion pit. The prefatigued SEM image illustrates the corrosion pit at the WT. The postfatigued image shows that two fatigue cracks initiated from the corrosion cracks and propagated along the same path of the continuous $κ_{III}$ phase. This supports the results found in [59]. Note that the images do not show the whole corrosion pit but focus on the deepest part of the pit.

3.3 | S-N Curves and Lifetime Prediction

By fitting a linear regression line to the experimental data for different classes of specimens, stress–life relationships were calculated in the form shown in Equation (5).

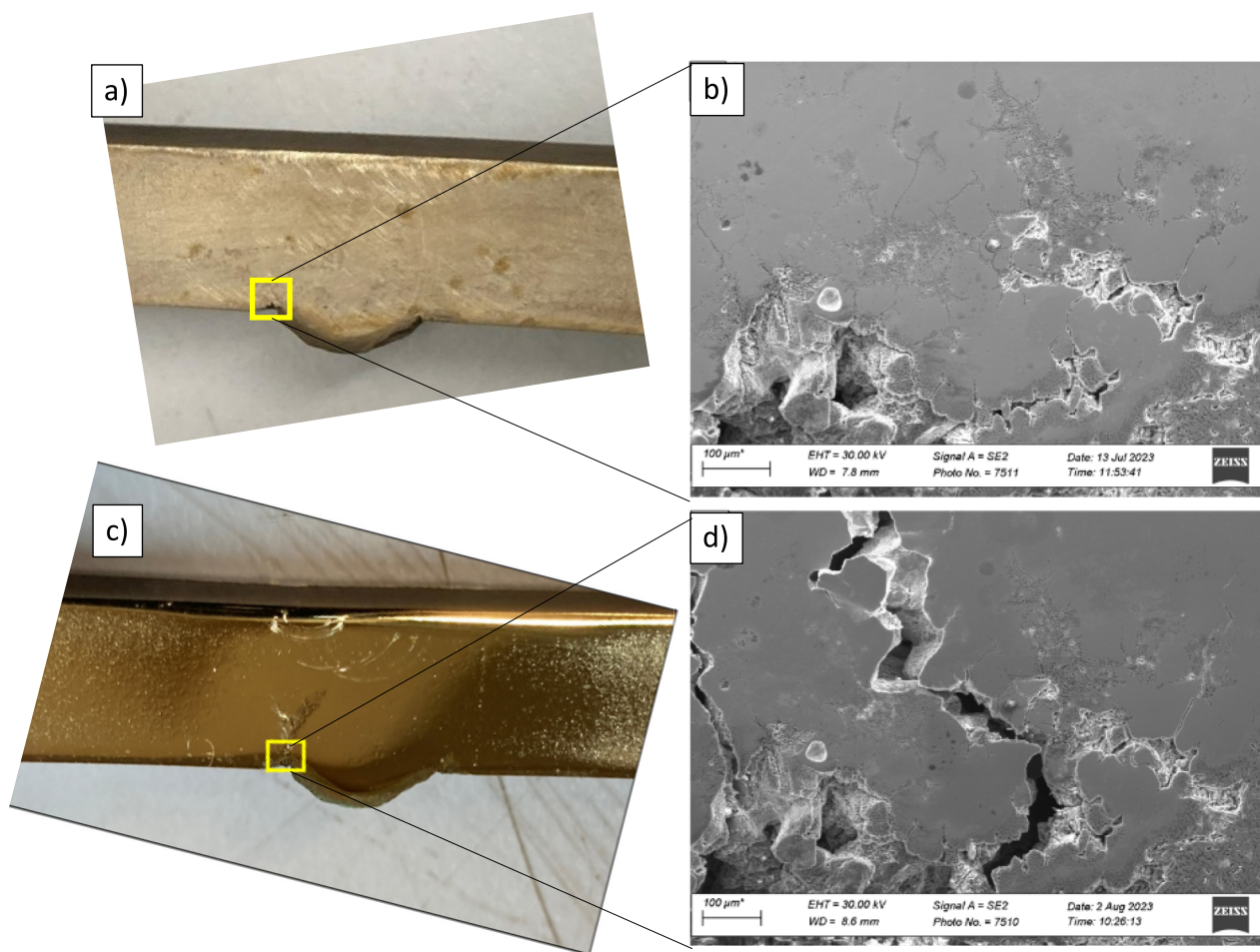$$\sigma_p = C_1 \, N^{C_2}$$

(5)

FIGURE 8 | (a) Photograph showing a fatigue sample cut from a coupon that had corroded in natural seawater (Millbay Marina, Plymouth) for 12 months (prior to polishing). (b) SEM image taken of the area highlighted in (a) showing stress corrosion cracking at the weld toe. (c) Another photograph of the same area of the same sample after polishing and after fatiguing to a peak stress of 220 MPa ($R = 0.1$, $f = 20$ Hz) for 6.4×10^4 cycles. (d) SEM image of the yellow area in (c) showing that fatigue cracks have initiated from the SPC paths seen in (b), along the κ_{III} phase. [Colour figure can be viewed at wileyonlinelibrary.com]

where σ_p = peak cyclic stress, C_1 and C_2 are constants calculated from the linear regression analysis, and N is the number of cycles to final fracture.

The parent samples had an S-N output similar to the heat-treated (HT) specimens in Mshana's 1984 study [20]. This was predictable as the HT in [20] was equivalent to Defense Standard 02-747 [3], experienced by the current parent samples. As such, the linear regression equation from the HT specimens in [20] can be compared with the linear regression from the parent samples here, Figure 9 and Table 5. The output from the present study is clearly similar to the output from the HT specimens in [20]. The perceived increase in fatigue resistance in the present samples was due to the difference in experimental conditions, in particular, Mshana's experiments used $R = -1$, whereas the current tests used $R = 0.1$. In addition, minor differences in the chemical composition and the improvement in HT conditions seen between 1984 and the present year will have altered the results.

The welded samples failed after fewer cycles compared with the parent samples in the same cyclic stress fatigue parameters.

The welded specimens where the weld bead had been ground off failed after fewer cycles compared with the parent samples, but more than the welded samples where the weld bead was still present (Table 5). Figure 10 shows the S-N curves for the following cases: parent (uncorroded) samples, welded (uncorroded) samples, welded and weld bead ground off (uncorroded) samples, and corroded welded samples.

The fatigue strength of natural seawater corroded samples at any given stress range was more variable than the uncorroded, SSW-immersed, and air-exposed (welded) cases, Figure 10. Natural seawater corroded samples had considerably less fatigue strength compared with SSW corroded samples because of the significantly more severe corrosion seen in the natural seawater corroded samples, caused by the effect of biofouling and the variable physiochemistry of natural seawater. This is addressed by Dobson et al. [6, 48].

The reduction in fatigue strength of natural seawater corroded samples correlated with the maximum depth of corrosion at the WT, whereas the pit aspect ratio (the ratio of pit depth to semiwidth) had no correlation. Therefore, the S-N curve for
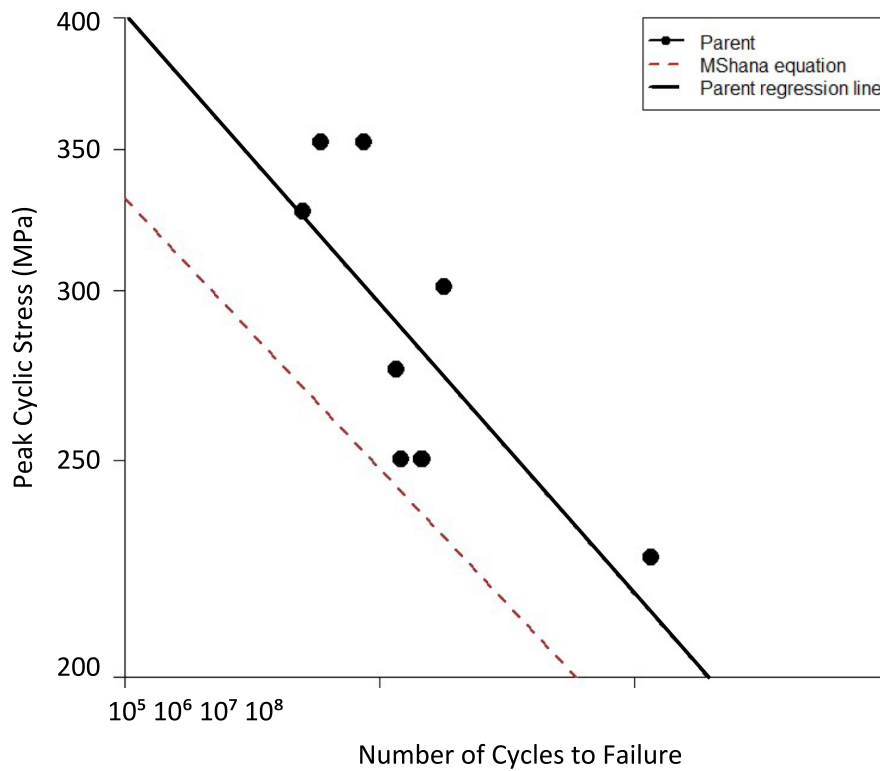
FIGURE 9 | S-N graph for the parent material showing the linear regression from the tested samples against the linear regression published by Mshana [20]. [Colour figure can be viewed at wileyonlinelibrary.com]
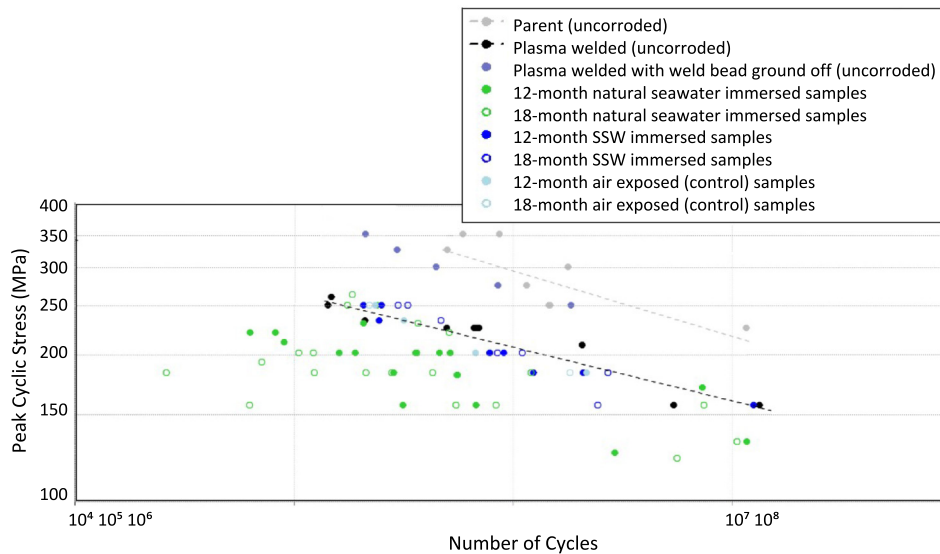

FIGURE 10 | S-N curve for parent (uncorroded) samples, welded (uncorroded) samples, welded with weld bead ground off (uncorroded) samples, and corroded welded samples. Linear trendlines are shown only for the uncorroded parent and welded cases. [Colour figure can be viewed at wileyonlinelibrary.com]

the natural seawater immersed samples was replotted with the samples classified by depth of WT corrosion. For this purpose, fatigue samples were defined by the maximum corrosion depth as per [42] using depth = 0.2 mm as a demarcation for "deep" pits (depth ≥ 0.2 mm) and pits with depth < 0.2 mm categorized as "shallow" pits. The resulting plot is shown in Figure 11.

3.4 | Short Crack Growth Model and Lifetime Predictions

We can improve the predictions from a simple corrective co-efficient using the SCGM prediction method described in [34, 58, 60].

To demonstrate the accuracy of the model, five corroded fatigue samples were chosen at random (using samples that had been immersed in natural seawater for 12 [$n=2$] and 18 [$n=3$] months). The corrosion depth and extent at the WTs of each of these samples were measured (Corrosion pits A–E, Table 4) and

the deepest corrosion pit was input into the SCGM in each case. The input data assumed that the width of the corrosion was the extent of the corrosion out from the WT (and not the width of the fatigue sample). Figure 12 shows the experimental results compared with the SCGM results for the five pits A–E.

When compared with experimentally obtained curves, model predictions are within 30% of experimental results.

TABLE 5 | Linear regression line coefficients (Equation 3) for cast and heat-treated NAB.

Samples	C_1	C_2
Heat-treated specimens from [20]	1390	−0.125
Parent NAB	1874	−0.134
Welded NAB	937	−0.110
Welded NAB with weld bead ground off	2208	−0.153

4 | Discussion

A key difference between the present experimental method and common corrosion fatigue experiment methodology is that all the fatigue tests were performed in air post–environmental exposure. This was done to consider the geometric effect that prior corrosion features have on fatigue strength. Consequently, these tests intentionally remove the effect of
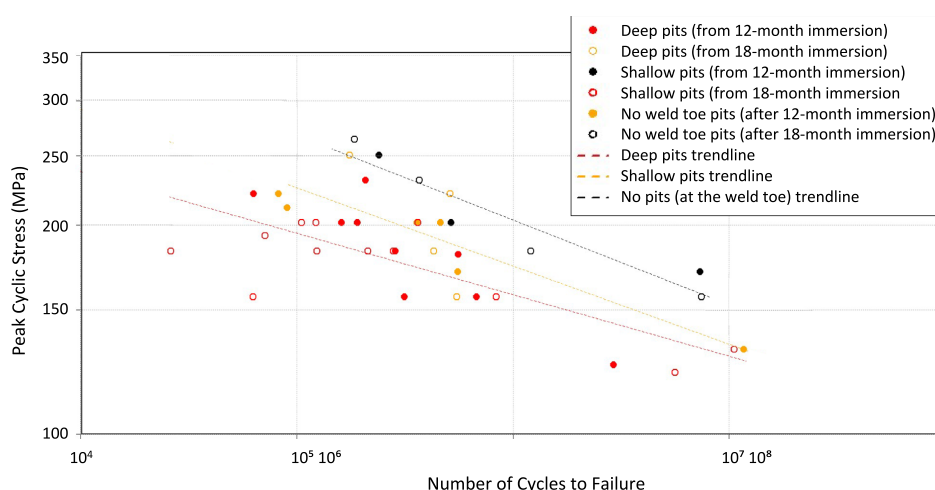

FIGURE 11 | S-N curve for samples that had been immersed in natural seawater for 12 or 18 months (shown as filled or unfilled circles, respectively). The number of cycles to failure is affected by maximum pit depth at the weld toe. Where "deep pits" have a depth of $\geq 0.2\,mm$ and "shallow pits" have a depth of $< 0.2\,mm$. The trendlines amalgamate 12- and 18-month immersion periods. [Colour figure can be viewed at wileyonlinelibrary.com]
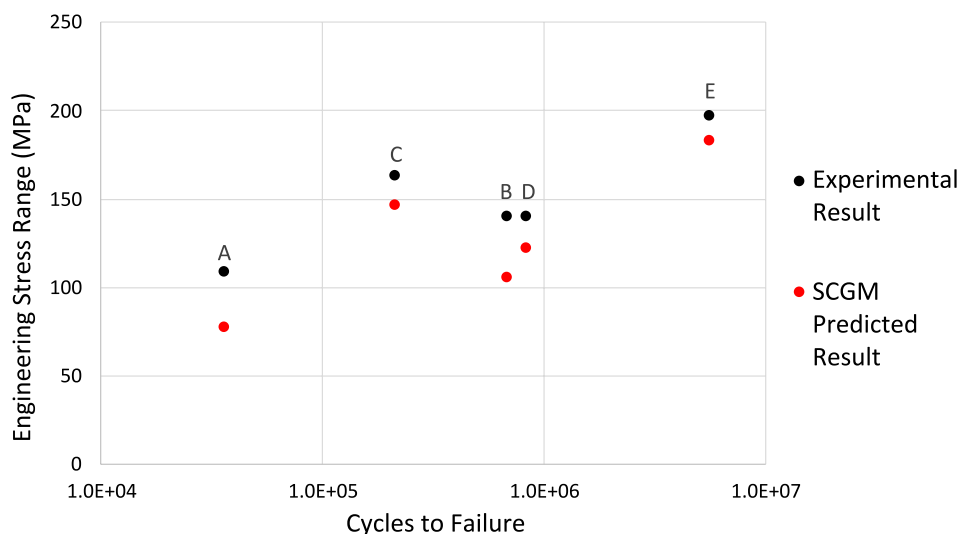

FIGURE 12 | SCGM predicted output vs experimental results for a sample of five Corrosion pits A–E, Table 4. [Colour figure can be viewed at wileyonlinelibrary.com]

the chemical action of the corrosive environment on the fatigue cracking process itself. However, in most service situations, the fatigue cycles will take place over a finite time (between maintenance or dry-docking periods) during which time the component is often continuously exposed to (or immersed in) seawater.

4.1 | Fatigue Crack Initiation and Propagation

It is well established that fatigue cracks initiate in areas where macroscopic stress risers, such as geometric discontinuities, are present [61]. In support of this, the WT was the point of failure in every welded sample ($n = 74$, uncorroded and corroded data combined).

To investigate the effect of weld bead geometry on fatigue strength, five welded samples were produced where the weld bead had been ground off. The results of these fatigue tests are shown as the purple values in Figure 10. These "ground" samples failed away from the WT, within the parent material. This suggests that geometry has a significant effect on fatigue failure initiation in uncorroded samples. These "ground" samples showed a fatigue strength that was higher than the welded samples, but still lower than the (unwelded) parent material. This suggests that, although geometric effects affect crack initiation, other affects cause reduced fatigue strength compared with the parent material. These additional effects include welding-induced RS and microstructural changes in the HAZ, which were both measured in the samples used in this study as described in [6].

The WM and HAZ contained the retained β' phase as observed in [16] when using gas metal arc welding on NAB. This phase is undesirable because of its susceptibility to selective phase corrosion (SPC), increased hardness, and brittleness [16]. For uncorroded samples, the microscopy results (Figures 5 and 6) show cracks propagating through the β' phase within the HAZ and through the κ_{III} phase outside the HAZ; this supports the results of [62] who showed fatigue cracks propagating between the α and κ_{III} phases in notched NAB samples. The complexity of the crack geometry seen in the x-ray CT images (e.g., Figure 7) further supports this phase selective propagation route.

Previous research by Xu et al. [63] suggested that interphase stress develops between phases in NAB to accommodate differential plastic deformation. They showed the softer α grains deforming plastically, whereas the harder grains behaved more elastically. As a result, the cracks propagate through areas of β' or κ_{III} phases, as these regions will be harder and therefore more vulnerable to brittle fracture. This crack propagation mechanism is best seen at the crack tip (e.g., Figure 6a) as, in wider sections of the crack, the κ_{III} phase fragments that remain on the surface of the fracture cleavage tend to be small (as seen in Figure 6b and in [62]).

It is well understood that fatigue cracks can initiate from corrosion cracks and pits [26–29]; however, cracks do not always initiate from the deepest point in the pit [64, 65]. The results show that (for NAB corroded in natural seawater) both fatigue crack propagation and corrosion crack propagation were along

the path of the β' phase within the HAZ and κ_{III} phase outside of the HAZ (Figures 6 and 8). This means that local areas of SPC could act as preinitiated crack sites in material that is subsequently cyclically loaded and consequently experiences fatigue cracking.

4.2 | The Effect of WT Corrosion Pit Geometry

Previous research [42] analyzed semielliptical, U-shaped, and V-shaped pits. These pits had varying depths (d) and aspect ratios (AR = semiwidth/d) and were used to assess the effect of depth and AR on fatigue strength. The results of [42] suggest that fatigue strength is controlled by depth for relatively shallow pits ($d < 0.2$ mm), whereas, for pits with depth of ≥ 0.2 mm, AR and depth can have a mixed influence on fatigue strength.

In the present results, the demarcation of fatigue behavior at $d = 0.2$ mm that samples with "deep" corrosion pits ($d \geq 0.2$ mm) had reduced fatigue strengths compared with samples with "shallow" corrosion pits ($d < 0.2$ mm) (Figure 11). This illustrates the significance of corrosion pit depth on fatigue strength.

AR was not found to have a significant effect on fatigue strength in either the shallow or deep cases. This is in agreement with [42] for the shallow samples but seems to be in contradiction for the deep samples. However, in the deep case, the correlation of fatigue strength with pit depth could have been due to the linear correlation seen between pit depth and AR, where AR reduced as pit depth increased (Figure 13). In addition, the results of [42] assume V-shaped, U-shaped, or semielliptical pits, whereas the current results are taken from real pits developed in natural seawater in the presence of natural environmental variables (including biofouling) and therefore present complex and varying morphologies. The complex topography of real corrosion pits in NAB has been shown to increase stress concentration within the pit [66]. These stress
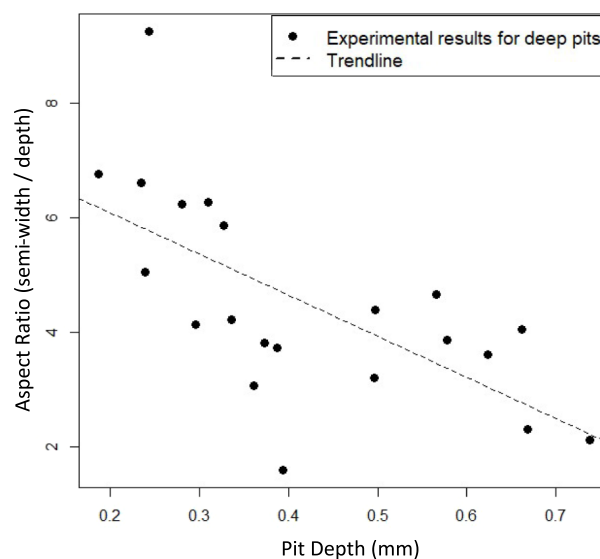
FIGURE 13 | Linear correlation seen between corrosion pit depth and aspect ratio (AR) for all pits with a pit depth of ≥ 0.2 mm (i.e., the "deep" pits). [Colour figure can be viewed at wileyonlinelibrary.com]

concentration factors could have effectively reduced the fatigue strength in samples with real corrosion pit topography more than the reduction seen in samples with V-shaped, U-shaped, or semielliptical pit geometry.

4.3 | Revalidation of NAB Components and the Wall Thickness Method

Wall thickness is often used as a minimum requirement in engineering standards applicable to copper alloy systems in contact with natural seawater, for example, Defense Standard 02-872 Part 3, BS MA 18:1973 and ASTM E8/E8M. As the fatigue samples were cut into 8-mm sections, the deep WT pits represent a minimum 4% wall thickness reduction (pit depth ≥ 0.35 mm). This is significant as Defense Standard 02-872 Part 3 (Issue 1) allows a 10% wall thickness reduction when revalidating seawater corroded NAB components (this thickness reduction is represented by pits with depth of ≥ 0.80 mm in this case). All the deep pits illustrated in this research would be allowable during the Defense Standard 02-872 Part 3 revalidation process, meaning that any NAB component showing these "deep pits" could (by the allowances of this Defense Standard) be re-used in a service environment where it is immersed in seawater. This means that the fatigue strength reduction seen in the samples with the deep pits could also be seen in components in service after revalidation by Defense Standard 02-872 Part 3.

The minimum wall thickness of the corrosion-pitted samples was calculated for the current results, allowing the stress experienced at the thinnest part of the sample to be recalculated with the reduced area. This peak stress was replotted against the number of cycles to failure (Figure 14) to produce a worst-case wall thickness reduction peak stress. The resulting figure shows that the wall thickness method does not completely account for the reduced fatigue strength in corrosion-pitted NAB. Although using the maximum corrosion pit depth to calculate wall thickness reduction is a simplification and a conservative approach, the fact that it still overpredicts fatigue strength proves that the conservativism is valid and, in fact, not conservative enough.

This is possibly due to the subsurface (and sub–corrosion pit) corrosion features that are not included in wall thickness estimates calculated using corrosion pit depth. For example, the corrosion cracks follow the path of the κ_{III} phase as described in [6]. This suggests that subsurface corrosion features have a significant impact on fatigue strength, so the wall thickness reduction method used in isolation could lead to overestimations of fatigue life.

Previous research has shown that subsurface corrosion features can be evaluated using techniques including mass loss estimates (that enable the calculation of corrosion rates) [67], electrical resistance methods [68], electromagnetic sensors (such as pulse-modulation eddy current imaging [69]), ultrasonic sensors [70], fiber-optic corrosion sensors [71], or radiographic sensors [72]. However, in industry, corrosion detection must monitor the entire component (or asset) and cannot just focus on a small area; therefore, some of these techniques are impractical for use by industry for in situ measurements. Each industrial application will have specific requirements in terms of budget, size and physical location of component(s), and frequency of inspections. Therefore, different commercially available sensors may be suitable in each case. A recent review [67] suggested that current developments in corrosion detection techniques have improved detection accuracy. The results of the current study suggest that, whenever possible, these commercially available, real-time, in situ, wireless communication subsurface corrosion
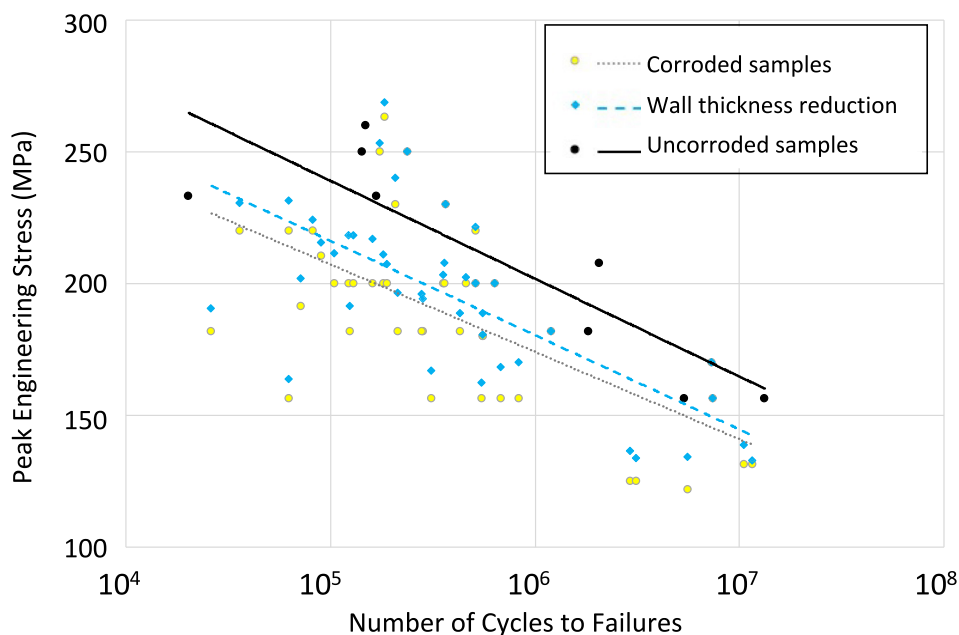

FIGURE 14 | S-N curve showing that taking wall thickness reduction into account by using maximum corrosion pit depth at the weld toe did not sufficiently address the reduced fatigue strength in the corroded samples compared with the uncorroded samples. [Colour figure can be viewed at wileyonlinelibrary.com]

sensors should be utilized by industry. This would avoid over-estimating fatigue lift through using the wall-thickness method for revalidation and potentially reduce the occurrence of premature failure.

4.4 | Fatigue Life Prediction

Using Figure 10, we compare the fatigue behavior of the parent, plasma welded, and corroded samples using a corrective coefficient [73], or KDF [21] using predictions from the linear regression models of the trendlines (shown in Figures 10 and 11). The knockdown range for the extreme stress inputs was calculated, and the KDF was taken as the average of the knockdown range. Table 6 shows the mean KDF calculated from the predicted linear models based on "Method 2" as described in [21]. The KDFs are calculated against the welded samples unless otherwise stated.

TABLE 6 | Mean and design knockdown factor (KDF) calculations based on "Method 2" in [21] when compared with the welded sample (unless otherwise stated).

Curve	Mean KDF
Welded	20.32 (compared with parent sample)
Air exposed (12 or 18 months)	1.26
SSW immersed (12 or 18 months)	1.20
12 months of natural seawater immersed	5.81
18 months of natural seawater immersed	10.89

The results shown in Table 6 suggest that, to make safe, conservative assumptions, we should assume the worst-case scenario and apply a KDF of 11 to any welded NAB component that has been immersed in natural seawater for 12–18 months. However, as these results do not include the fatigue crack propagation because of the chemical effect of seawater during cyclic loading, the effect of this needs to be included in any holistic KDF calculation. In addition, as fatigue life is a statistical quantity, with additional factors such as casting defects, that can also reduce fatigue life [74], KDFs must be inherently conservative. This KDF assumes that a weld bead is present and that no bending stresses exist.

Using a KDF of 11 could be a quick, high-level, order-of-magnitude method to estimate the lifetime of multiple components (e.g., at the "rough order of magnitude" [ROM] quotation stage). However, it could lead to the removal of corroded NAB components or assets earlier than necessary. This would cause unnecessary material wastage, with associated cost implications and detrimental environmental consequences. As sustainable engineering practices require the reduction of unnecessary metal waste, an alternative approach is suggested using the SCGM.

Figure 12 shows that the SCGM predictions (based on Chapetti's description of the K-T diagram [41]) are reliable for a range of corrosion pit depths and stress ranges. The model produces consistent life values that are moderately conservative. This conservativism is seen to be slightly increased for deeper pits (as the difference in the predicted value and the experimental value is larger for deeper pits), with a strong linear trend shown in Figure 15. The corrosion process within the marine environment is highly variable and stochastic because of the vast number of interacting factors (including seawater temperature, salinity, flow rate, and biofouling). As such, the correlation shown in Figure 15 is advantageous as it creates an increase in conservatism as risk increases (due to increased stress concentration in deeper pits). In addition, the SCGM requires very few
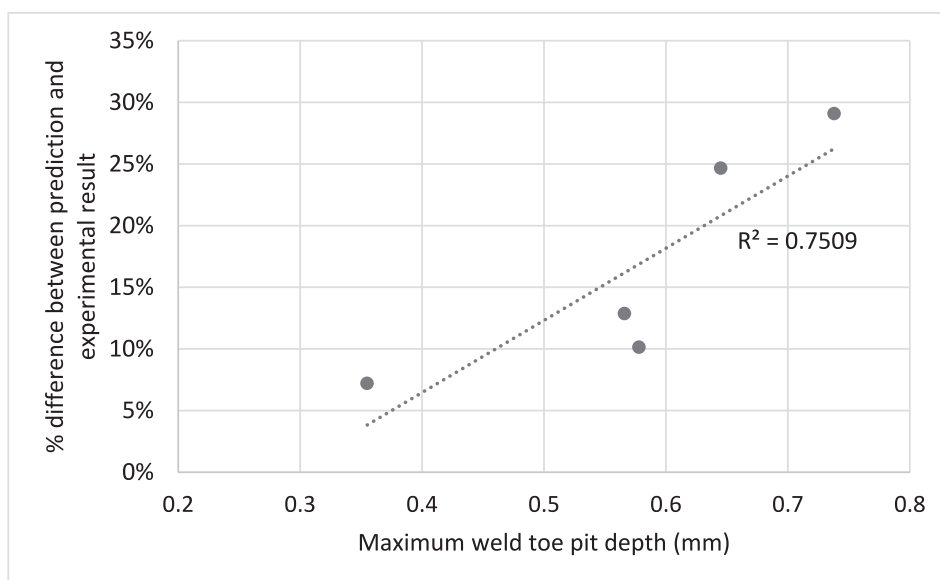
FIGURE 15 | Percentage difference between the SCGM predictions and the experimental results against the maximum WT pit depth (mm).

input parameters thus providing a good balance between accuracy and effort.

This SCGM could significantly improve the failure prediction of components where corrosion is observed at a loaded WT. It demonstrates a predictive model for fatigue life that is accurate and reliable and can be easily applied by the marine industry using off-the-shelf tools, thus fulfilling a gap identified in [75]. This could significantly improve the failure prediction of corroded, welded, and loaded components and could be used as a tool for the revalidation of corroded NAB.

5 | Conclusions

For corroded NAB, the fatigue behavior was found to be influenced by the depth of corrosion at the WT. It is suggested that for welded NAB immersed in the natural marine environment for up to 18 months and showing corrosion at the WT, a KDF of at least 11 should be applied when estimating fatigue life based on uncorroded S-N curves.

A number of current engineering standards use a wall thickness reduction method to calculate fatigue strength reduction of corroded material. However, the results show that the wall thickness reduction method in isolation overestimates fatigue strength.

Corrosion cracks and fatigue cracks both propagate along the path of the β' and κ_{III} phases. Corrosion pit morphological complexity also creates stress concentrations that exacerbate weld-induced residual stress at the WT. Fatigue strength predictions can be achieved by knowing material parameters and WT corrosion pit geometry.

From these results, it may be concluded that the revalidation processes currently used for seawater corroded NAB are non-conservative. The results show a significant reduction in fatigue strength for wall thickness reductions less than those allowed by the current revalidation processes and suggest a corrosion rate higher than that currently assumed by the standards.

To solve this, the SCGM produces accurate and reliable fatigue life predictions that could be easily applied by industry to aid in revalidation decision making and inspection scheduling.

Author Contributions

Tamsin Dobson: conceptualization, data curation, methodology, investigation, formal analysis, writing–original draft, writing–review and editing, funding. **Paul Wilson:** CT data curation, CT investigation. **Nicolas Larrosa:** validation, writing–review and editing, supervision. **Mark Williams:** CT supervision. **Harry Coules:** validation, writing–review and editing, supervision, funding.

Data Availability Statement

The data that support the findings of this study are available from the corresponding author upon reasonable request.

References

1. Marine Accident Investigation Branch, *Flooding and Foundering of the Fishing Vessel Ocean Quest (FR 375) 70 Miles North-East of Fraserburgh on 18 August 2019* (Southampton: MAIB, 2021).

2. Marine Accident Investigation Branch, "Report on the Investigation of Ferry, a Fire on Board the RoPax Dieppe Seaways on the Approach to, and Subsequently alongside the Port of Dover, UK 2014, on 1 May. Southampton," (2015).

3. Ministry of Defence, "Defence Standard 02-747 Part 2 Requirements for Nickel Aluminium Bronze Castings and Ingots Part 2: Nickel Aluminium Bronze Naval Alloy Ingots and Sand Casting with Welding Permitted to the Wetted Surface," (2013).

4. P. Kucharczyk, M. Madia, U. Zerbst, B. Schork, P. Gerwien, and S. Münstermann, "Fracture-Mechanics Based Prediction of the Fatigue Strength of Weldments. Material Aspects," *Engineering Fracture Mechanics* 198 (2018): 79-102.

5. H. Pasek-Siurek, "Plasma Welding: Processes and Equipment," *Welding International* 28 (2014): 672-678.

6. T. Dobson, N. Larrosa, M. Reid, K. Rajamudili, S. Ganguly, and H. Coules, "Corrosion Mechanisms of Plasma Welded Nickel Aluminium Bronze Immersed in Seawater," *Corrosion Science* 232 (2024): 112004.

7. D. R. Lenard, C. J. Bayley, and B. A. Noren, "Electrochemical Monitoring of Selective Phase Corrosion of Nickel Aluminum Bronze in Seawater," *Corrosion* 64, no. 10 (2008): 764-772.

8. A. Jahanafrooz, F. Hasan, G. Lorimer, and N. Ridley, "Microstructural Development in Complex Aluminium Bronzes," *Metallurgical Transactions a* 14 (1983): 1951-1956.

9. D. Bell, T. Marsico, K. Petrolonis, P. Denney, and P. Howell, "The Microstructure of Laser-Welded Aluminum Bronzes," in *Metallography: Past, Present, and Future (75th Anniversary Volume)*, eds. G. Vander Voort, F. Warmuth, S Purdy, and A Szirmae (West Conshohocken, PA: ASTM International, 1993).

10. E. Skilbred, *Corrosion of NAB in Seawater* (PhD thesis, Norwegian University of Science and Technology, 2016).

11. R. Cottam, V. Luzin, H. Moody, et al., "The Role of Microstructural Characteristics in the Cavitation Erosion Behaviour of Laser Melted and Laser Processed Nickel-Aluminium Bronze," *Wear* 317 (2014): 56-63.

12. D. Nakhaie, A. Davoodi, and A. Imani, "The Role of Constituent Phases on Corrosion Initiation of NiAl Bronze in Acidic Media Studied by SEM–EDS, AFM and SKPFM," *Corrosion Science* 80 (2014): 104-110.

13. E. A. Culpan and G. Rose, "Microstructural Characterisation of Cast Nickel Aluminium Bronze," *Journal of Materials Science* 13 (1978): 1647-1657.

14. M. Hazra and K. P. Balan, "Failure of a Nickel Aluminium Bronze (NAB) Canned Motor Pump Impeller Working Under Polluted Sea Water—Influence of Material Selection, Section Thickness Dependent Microstructure and Temper Annealing Heat Treatment," *Engineering Failure Analysis* 70 (2016): 141-156.

15. T. Murray, S. Thomas, Y. Wu, W. Neil, and C. Hutchinson, "Selective Laser Melting of Nickel Aluminium Bronze," *Additive Manufacturing* 33 (2020): 101122.

16. H. Li, D. Grudgings, N. P. Larkin, J. Norrish, M. Callaghan, and L. Kuzmikova, "Optimization of Welding Parameters for Repairing NiAl Bronze Components," *Materials Science Forum* 706–709 (2012): 706-709.

17. C. Dharmendra, A. Hadadzadeh, B. S. Amirkhiz, G. D. Janaki Ram, and M. Mohammadi, "Microstructural Evolution and Mechanical Behavior of Nickel Aluminum Bronze Cu-9Al-4Fe-4Ni-1Mn Fabricated Through Wire-Arc Additive Manufacturing," *Additive Manufacturing* 30 (2019): 100872.

18. ASM International Handbook Committee, *Fatigue and Fracture*, vol. 19 (USA: ASM International, 1996).

19. K.-S. Park and S. Kim, "Corrosion and Corrosion Fatigue Characteristics of Cast NAB Coated With NAB by HVOF Thermal Spray," *Journal of the Electrochemical Society* 158 (2011): C335.

20. J. Mshana, O. Vosikovsky, and M. Sahoo, "Corrosion Fatigue Behaviour of Nickel-Aluminum Bronze Alloys," *Canadian Metallurgical Quarterly* 23 (1984): 7-15.

21. C. M. Holtam, C. R. A. Schneider, and G. Slater, "Best Practice Guidance for Evaluating Knock-Down Factors in Corrosive Environments," *Proceedings of the International Conference on Offshore Mechanics and Arctic Engineering - OMAE* 6 (2012): 129-136.

22. Q. Han, Y. Li, Y. Lu, and G. Wang, "Effect of Corrosion on the Fatigue Crack Propagation Properties of Butt Weld With G20Mn5QT Cast Steel and Q355D Steel in 3.5-wt% NaCl Solution," *Fatigue and Fracture of Engineering Materials and Structures* 46 (2023): 4020-4035.

23. V. Okenyi, S. Afazov, N. Mansfield, et al., "Corrosion Surface Morphology-Based Methodology for Fatigue Assessment of Offshore Welded Structures," *Fatigue and Fracture of Engineering Materials and Structures* 46 (2023): 4663-4677.

24. T. Shiozaki, N. Yamaguchi, Y. Tamai, J. Hiramoto, and K. Ogawa, "Effect of Weld Toe Geometry on Fatigue Life of Lap Fillet Welded Ultra-High Strength Steel Joints," *International Journal of Fatigue* 116 (2018): 409-420.

25. E. Niemi, "Stress Raisers," in *Stress Determination for Fatigue Analysis of Welded Components* (Cambridge, England: Woodhead Publishing, 1995), 12-18.

26. T. C. Lindley, P. Mcintyre, and P. J. Trant, "Fatigue-Crack Initiation at Corrosion Pits," *Materials Technology* 9 (1982): 135-142.

27. S. I. Rokhlin, J.-Y. Kim, H. Nagy, and B. Zoofan, "Effect of Pitting Corrosion on Fatigue Crack Initiation and Fatigue Life," *Engineering Fracture Mechanics* 62 (1999): 425-444.

28. X. Zhang, S. Li, R. Liang, X. Zhang, S. Li, and R. Liang, "Effect of Corrosion Pits on Fatigue Life and Crack Initiation," in *ICF13* (Beijing: The Chinese Society of Theoretical and Applied Mechanics, 2013).

29. V. Sabelkin, V. Y. Perel, H. E. Misak, E. M. Hunt, and S. Mall, "Investigation Into Crack Initiation From Corrosion Pit in 7075-{T6} Under Ambient Laboratory and Saltwater Environments," *Engineering Fracture Mechanics* 134 (2015): 111-123.

30. O. Fatoba and R. Akid, "On the Behaviour of Small Fatigue Cracks Emanating From Corrosion Pits: Part I—The Influence of Mechanical Factors," *Theoretical and Applied Fracture Mechanics* 117 (2022): 103154.

31. Q. Wang, "Effect of Pitting Corrosion on Very High Cycle Fatigue Behavior," *Scripta Materialia* 49 (2003): 711-716.

32. H. Qi, Y. Lu, S. Song, and Q. Xu, "Fatigue Reliability Analysis System for Key Components of Aero-Engine. Xu J, ed," *International Journal of Aerospace Engineering* 2022 (2022): 1143901.

33. C. Luo and A. Chattopadhyay, "Prediction of Fatigue Crack Initial Stage Based on a Multiscale Damage Criterion," *International Journal of Fatigue* 33 (2011): 403-413.

34. A. Navarro and E. R. D. L. Rios, "Short and Long Fatigue Crack Growth: A Unified Model," *Philosophical Magazine A* 57 (1988): 15-36.

35. W. L. Morris, "The Noncontinuum Crack Tip Deformation Behavior of Surface Microcracks," *Metallurgical Transactions A* 11 (1980): 1117-1123.

36. J. Lankford, "The Influence of Microstructure on the Growth of Small Fatigue Cracks," *Fatigue and Fracture of Engineering Materials and Structures* 8 (1985): 161-175.

37. E. O. Hall, "The Deformation and Ageing of Mild Steel: III Discussion of Results," *Proceedings of the Physical Society. Section B* 64 (1951): 747-753.

38. N. J. Petch, "The Cleavage Strength of Polycrystals," *Journal of the Iron and Steel Institute* 174 (1953): 25-28.

39. H. Kitagawa and S. Takahashi, "Applicability of Fracture Mechanics to Very Small Cracks or the Cracks in the Early Stage," in *Proceedings 2nd International Conference on Mechanical Behaviour of Materials* (Boston, Massachusetts, 1976), 627-631.

40. M. Benedetti and C. Santus, "Building the Kitagawa-Takahashi Diagram of Flawed Materials and Components Using an Optimized V-Notched Cylindrical Specimen," *Engineering Fracture Mechanics* 224 (2020): 106810.

41. M. D. Chapetti, "Fatigue Propagation Threshold of Short Cracks Under Constant Amplitude Loading," *International Journal of Fatigue* 25 (2003): 1319-1326.

42. J. A. A. Balbín, V. Chaves, and N. O. O. Larrosa, "Pit to Crack Transition and Corrosion Fatigue Lifetime Reduction Estimations by Means of a Short Crack Microstructural Model," *Corrosion Science* 180 (2021): 109171.

43. V. Chaves and A. Navarro, "Fatigue Limits for Notches of Arbitrary Profile," *International Journal of Fatigue* 48 (2013): 68-79.

44. E. A. Culpan and A. G. Foley, "The Detection of Selective Phase Corrosion in Cast Nickel Aluminium Bronze by Acoustic Emission Techniques," *Journal of Materials Science* 17 (1982): 953-964.

45. R. S. Oakley, J. C. Galsworthy, G. S. Fox, and K. R. Stokes, "Long-Term and Accelerated Corrosion Testing Methods for Cast Nickel-Aluminium Bronzes in Seawater," in *Corrosion Behaviour and Protection of Copper and Aluminium Alloys in Seawater* (Cambridge, England: Woodhead Publishing, 2007), 119-127.

46. J. A. Wharton and K. R. Stokes, "The Influence of Nickel-Aluminium Bronze Microstructure and Crevice Solution on the Initiation of Crevice Corrosion," *Electrochimica Acta* 53 (2008): 2463-2473.

47. J. A. Wharton, R. C. Barik, G. Kear, R. J. K. Wood, K. R. Stokes, and F. C. Walsh, "The Corrosion of Nickel-Aluminium Bronze in Seawater," *Corrosion Science* 47 (2005): 3336-3367.

48. T. Dobson, A. Yunnie, D. Kaloudis, N. Larossa, and H. Coules, "Biofouling and Corrosion Rate of Welded Nickel Aluminium Bronze in Natural and Simulated Seawater," *Biofouling* 40, no. 2 (2024): 1-16.

49. C. E. Jaske, D. A Utah, W. K. Boyd, Corrosion Fatigue of Cast Propeller Alloys. *SNAME Propellers'78 Symp.* May 1978: D011S001R003.

50. M. Prager, "The Properties of Cast Alloys for Large Marine Propellers," in *American Society of Mechanical Engineers. Cast Metal for Structural and Pressure Containment Applications* (New York, NY: ASME, 1979), 225-302.

51. V. Cnudde and M. N. Boone, "High-Resolution X-Ray Computed Tomography in Geosciences: A Review of the Current Technology and Applications," *Earth-Science Reviews* 123 (2013): 1-17.

52. H. Nakazawa and S. Kodama, "Statistical S-N Testing Method With 14 Specimens: JSME Standard Method for Determination of S-N Curves," in *Statistical Research on Fatigue and Fracture* (New York: Elsevier Applied Science, 1987), 59-69.

53. The British Standards Institution *BS 7608: 2014+A1:2015—Guide to Fatigue Design and Assessment of Steel Products* (London, England: The British Standards Institution, 2015).

54. N. O. Larrosa, A. Navarro, and V. Chaves, "Calculating Fatigue Limits of Notched Components of Arbitrary Size and Shape With Cracks Growing in Mode I," *International Journal of Fatigue* 74 (2015): 142-155.

55. A. Navarro and E. R. de los Rios, "An Alternative Model of the Blocking of Dislocations at Grain Boundaries," *Philosophical Magazine A* 57 (1988): 37-42.

56. T. Dobson, N. Larrosa, S. Kabra, and H. Coules, "The Role of Surface Roughness on Pitting Corrosion Initiation in Nickel Aluminium Bronzes in Air," *Proceedings International Conference on Offshore Mechanics and Arctic Engineering - OMAE* 3 (2022): 1-12.

57. E. J. Czyrycs, "Corrosion Fatigue Crack Growth Thresholds for Cast Nickel-Aluminum Bronze and Welds," in *Fatigue Crack Growth Thresholds, Endurance Limits and Design*, eds. J. C. Newman and R. S. Piascik (ASTM STP 1. West Conshohocken, PA, 2000: American Society for Testing and Materials, 2020), 319.

58. N. O. Larrosa, "A Dislocation Based Method Using Generative Algorithms to Model Notch Geometries: Determination of Mode I SIFs," *Engineering Fracture Mechanics* 127 (2014): 327-335.

59. Y. Ding, R. Zhao, Z. Qin, et al., "Evolution of the Corrosion Product Film on Nickel-Aluminum Bronze and Its Corrosion Behavior in 3.5 wt % NaCl Solution," *Materials (Basel).* 12 (2019): 209.

60. M. Bergant, N. O. Larrosa, A. Yawny, and M. Madia, "Short Crack Growth Model for the Evaluation of the Fatigue Strength of WAAM Ti-6Al-4V Alloy Containing Pore-Type Defects," *Engineering Fracture Mechanics* 289 (2023): 109467.

61. U. Zerbst, "Application of Fracture Mechanics to Welds With Crack Origin at the Weld Toe: A Review Part 1: Consequences of Inhomogeneous Microstructure for Materials Testing and Failure Assessment," *Welding in the World* 63 (2019): 1715-1732.

62. X. Xu, Y. Lv, M. Hu, et al., "Influence of Second Phases on Fatigue Crack Growth Behavior of Nickel Aluminum Bronze," *International Journal of Fatigue* 82 (2016): 579-587.

63. X. Xu, H. Wang, Y. Lv, W. Lu, and G. Sun, "Investigation on Deformation Behavior of Nickel Aluminum Bronze by Neutron Diffraction and Transmission Electron Microscopy," *Metallurgical and Materials Transactions A, Physical Metallurgy and Materials Science* 47 (2016): 2081-2092.

64. E. P. Zarandi and B. H. Skallerud, "Cyclic Behavior and Strain Energy-Based Fatigue Damage Analysis of Mooring Chains High Strength Steel," *Marine Structures* 70 (2020): 102703.

65. P. Qvale, E. P. Zarandi, S. K. Ås, and B. H. Skallerud, "Digital Image Correlation for Continuous Mapping of Fatigue Crack Initiation Sites on Corroded Surface From Offshore Mooring Chain," *International Journal of Fatigue* 151 (2021): 106350.

66. T. Dobson, N. Larrosa, and H. Coules, "The Role of Corrosion Pit Topography on Stress Concentration," *Engineering Failure Analysis* 157 (2024): 107900.

67. M. S. B. Reddy, D. Ponnamma, K. K. Sadasivuni, et al., "Sensors in Advancing the Capabilities of Corrosion Detection: A Review," *Sensors and Actuators A: Physical* 332 (2021): 113086.

68. Y. Zhu, Y. Xu, S. Song, X. Wang, G. Liu, and Y. Huang, "Probing the Nonuniform Corrosion of Pipeline Weldments Under Stepwise Increasing Solution Temperature Using a Coupled Multielement Electrical Resistance Sensor," *Materials and Corrosion* 71 (2020): 1386-1399.

69. B. Yan, Y. Li, Z. Liu, S. Ren, I. M. Zainal Abidin, and Z. Chen, "Pulse-Modulation Eddy Current Imaging and Evaluation of Subsurface Corrosion via the Improved Small Sub-Domain Filtering Method," *NDT & E International* 119 (2021): 102404.

70. F. Zou and F. B. Cegla, "High-Accuracy Ultrasonic Corrosion Rate Monitoring," *Corrosion* 74 (2017): 372-382.

71. D. Luo, J. Li, and Y. Li, "A Review of Fiber-Optic Corrosion Sensor in Civil Engineering," *AIP Conference Proceedings* 1967 (2018): 20055.

72. K. Edalati, N. Rastkhah, A. Kermani, M. Seiedi, and A. Movafeghi, "The Use of Radiography for Thickness Measurement and Corrosion Monitoring in Pipes," *International Journal of Pressure Vessels and Piping* 83 (2006): 736-741.

73. P. P. Milella, "Factors That Affect S-N Fatigue Curves," in *Fatigue and Corrosion in Metals* (Springer Milano: Verlag, 2012), 109-191.

74. A. Sarkar, A. Chakrabarti, A. Nagesha, et al., "Influence of Casting Defects on S–N Fatigue Behavior of Ni-Al Bronze," *Metallurgical and Materials Transactions A : Physical Metallurgy and Materials Science* 46 (2015): 708-725.

75. N. O. Larrosa, R. A. Ainsworth, R. Akid, et al., "'Mind the Gap' in Fitness-For-Service Assessment Procedures-Review and Summary of a Recent Workshop," *International Journal of Pressure Vessels and Piping* 158 (2017): 1-19.

Supporting Information

Additional supporting information can be found online in the Supporting Information section.